Powder Technology 438 (2024) 119672

Contents lists available at ScienceDirect

Powder Technology

journal homepage: www.journals.elsevier.com/powder-technology

Unraveling grain growth of metallic tungsten: Investigating the nanoscale realm of hydrogen reduction of tungsten oxides

Alvaro A. Estupinan-Donoso [a,*], Pauline Gravier [b], Rodrigo U. Ichikawa [c], Andreas Michels [a]

[a] Department of Physics and Materials Science, Université du Luxembourg, 162a, avenue de la Faïencerie, L-1511, Luxembourg
[b] ESRF, The European Synchrotron Radiation Facility, 71 Avenue des Martyrs, CS 40220, 38043 Grenoble Cedex 9, France
[c] Materials Science and Technology Center (CCTM), Nuclear and Energy Research Institute (IPEN – CNEN), Ave. Lineu Prestes, 2242, Cidade Universitária, São Paulo - SP, 05508-000, Brazil

GRAPHICAL ABSTRACT

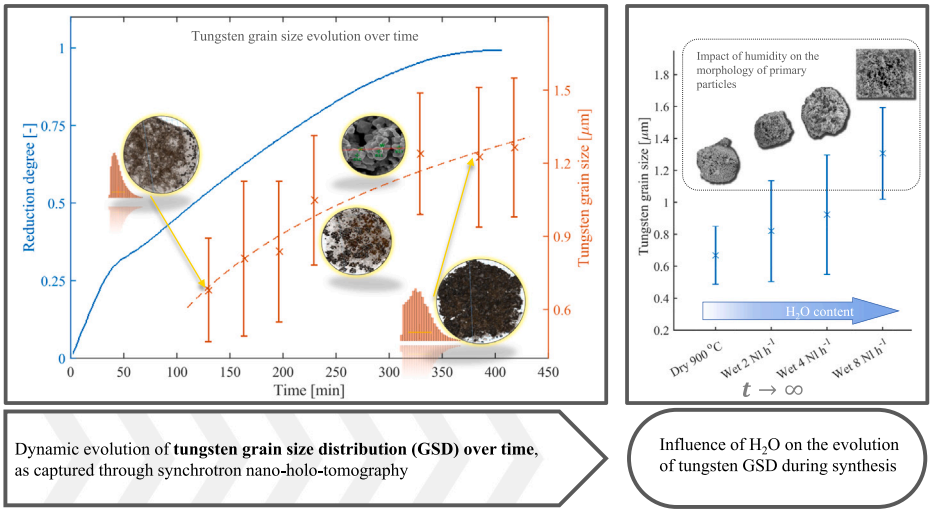

Dynamic evolution of **tungsten grain size distribution (GSD) over time**, as captured through synchrotron nano-holo-tomography

Influence of H_2O on the evolution of tungsten GSD during synthesis

HIGHLIGHTS

- Quasi-in-situ experimentation reveals evolving tungsten microstructure.
- Precise Grain Characterization via Synchrotron nanotomography and electron microscopy.
- Dynamic view of tungsten grain evolution during reduction, beyond final sizes.
- Redefine theories by emphasize H2O's role in particle fracture and reaction rates.
- Correlation between grain and crystallite growth, impacting academia and industry.

ARTICLE INFO

Keywords:
Tungsten trioxide reduction
Phase contrast imaging
In-situ reaction

ABSTRACT

This paper focuses on the experimental observation of tungsten grain evolution during the process of hydrogen reduction of tungsten trioxide. The objective is to gain insights into the grain size distribution (GSD) evolution and morphology changes of metallic tungsten. The study employs an amalgamation of conventional characterization techniques – such as TGA, SEM-EDS, TEM and XRD – alongside cutting-edge techniques

* Corresponding author.
E-mail address: alvaro@estupinan.net (A.A. Estupinan-Donoso).

https://doi.org/10.1016/j.powtec.2024.119672
Received 16 October 2023; Received in revised form 26 January 2024; Accepted 17 March 2024
Available online 19 March 2024

Grain size distribution
Grain growth

like phase contrast nano-tomography from synchrotron sources. Conducted as a quasi in-situ study, this research offers the opportunity to observe the transient evolution of the formed metallic tungsten phase within its precursor WO_2 particles. The paper presents and discusses quantitative results concerning the evolution of GSD and morphological changes, encompassing growth rates of both crystallites and grains of the synthesized metallic phase. Additionally, the quasi in-situ study highlights the dependence of grain size on water concentration during the reduction process. The qualitative and quantitative findings contribute to a more nuanced understanding of the kinetics of grain growth of metallic tungsten and offer insights into the intricate interplay between reduction parameters, GSD evolution and morphological changes. Gaining a deeper understanding of the underlying mechanisms driving the changes in GSD establishes a foundation for predictive theory with immediate academic and industrial impact.

1. Introduction

The evolution of Grain Size Distribution (GSD) and morphological changes in metallic tungsten during the process of hydrogen reduction of tungsten oxides plays a pivotal role in understanding its microstructural transformation and mechanical properties. The metallic tungsten grain size and morphology directly influence key properties, such as hardness and toughness, of final tungsten carbide (WC) products. Irregular large grains, for instance, may act as nucleation points for fracture [1,2]. Metallic tungsten is industrially produced through the hydrogen reduction of tungsten yellow oxide (WO_3) or tungsten blue oxide (TBO) (i.e., a mixture of oxides ranging from WO_3 to $WO_{2.98}$, [3]) at temperatures above 700 C. This process follows a well-defined sequence involving solid intermediates: $WO_3 \rightarrow WO_{2.98} \rightarrow WO_{2.9} \rightarrow WO_{2.72} \rightarrow WO_2 \rightarrow W$ [4]. Notably, the $WO_2 \rightarrow W$ step represents the longest and most critical stage, ultimately influencing the final properties of the obtained metallic tungsten [4–7].

Morphological changes occurring during the synthesis of metallic tungsten through hydrogen reduction of tungsten oxides have captured significant interest since the discovery of cemented carbides. The work of Sarin [8] marked the beginning of research efforts to understand the controlling factors influencing the grain size of tungsten. In subsequent studies, Wilken et al. [9] and Taskinen et al. [10,11] investigated the impact of dopants on the final size of the produced metallic tungsten. More recently, Wu et al. [12], also studied the contributions of dopants on the morphology of tungsten grains upon H_2 reduction. Over the years, numerous publications have delved into the influence of reducing conditions on the resulting size of tungsten grains. Early observations by Lackner et al. [13] revealed the prompt formation of pure tungsten grains and offered initial insights into the evolution of the morphology of the precursor oxide matrix. A comprehensive collection of reduction mechanisms and possible tungsten grain formation mechanisms was documented in a dedicated book on tungsten [4]. As pioneeringly stated by Belton and McCarron [14], the growth of tungsten grains is attributed to the formation of the volatile compound $WO_2(OH)_2$ under a Chemical Vapor Transport (CVT) process, which is produced in the presence of water vapor and later deposited on lower oxides. Recently, Matviichuk et al. [15] and Ostermann et al. [16,17], observed long-range deposition of $WO_2(OH)_2$, proving the influence of volatilization and deposition processes on the growth of metallic tungsten grains. Recently, Schoderbock [18], had conducted a microscale research study to better understand the evolution of solid intermediates in the course of the reduction. Wang et al. [7] provide qualitative observations regarding the impact of $WO_2(OH)_2$ on the coarsening of tungsten powder during industrial reduction processes. Their research, employing electron microscopy techniques, offers contributions to understanding the progression of intermediate solid oxides during reduction.

Despite decades of research, a lack of consensus exists on the kinetics of the reactions involved and a substantial discrepancy remains regarding how reduction conditions precisely affect the process. Moreover, the morphological evolution of tungsten grains after formation is not yet understood. The prevailing literature exclusively focuses on observations post full reduction, offering no insights into the morphology, sizes, or growth rates of newly formed W grains. Thus, a transient analysis of the morphological evolution of tungsten grains upon their formation would provide valuable insights into the process.

In this study, our objective is to present and discuss the quantitative results obtained from the characterization of GSD evolution and morphology changes occurring during hydrogen reduction of tungsten oxides. To achieve this, we employed a combination of conventional and state-of-the-art characterization techniques. The conventional techniques included Thermogravimetric Analysis (TGA), Scanning Electron Microscopy with Energy-Dispersive X-ray Spectroscopy (SEM-EDS), Transmission Electron Microscopy (TEM) for higher-resolution imaging, and X-ray Diffraction (XRD), which allowed for the determination of crystallite size distribution and the identification of the formed metallic phase. Additionally, three-dimensional (3D) measurements were performed using state-of-the-art X-ray phase contrast nano-holotomography (XNH) with synchrotron sources. By employing this advanced X-ray phase contrast technique, we obtained detailed 3D information that provided a comprehensive understanding of the evolution of the microstructure and size of the tungsten grains. This technique offered exceptional resolution, allowing for the non-destructive characterization of the internal structure of the samples. The obtained 3D information complements and enhances the insights gained from other more conventional characterization techniques, providing a more comprehensive and accurate analysis of the grain evolution of the metallic tungsten formation.

The obtained quantitative results reveal the dynamic evolution of the GSD throughout the hydrogen reduction process. We discuss the changes observed in the distribution profiles, highlighting the shifts in the mean grain size and the spread of the distribution. Furthermore, we present the morphology changes captured through electron microscopy, providing visual evidence of the structural transformations occurring during reduction. Of particular interest is the determination of growth rates for pure tungsten crystallites and grains formed within the oxide phase. By analyzing the temporal evolution of the GSD, it is possible to derive valuable insights into the kinetics of grain growth. Quantifying the growth rates enables a deeper understanding of the underlying mechanisms driving the GSD changes and providing a basis for process modeling and predictive theory.

The discussion of the quantitative results sheds light on the relationship between reduction parameters and the observed GSD evolution and morphology changes. We explore the influence of various factors such as temperature, time and hydrogen concentration over water concentration on the growth rates of crystallites and grains, providing a better understanding of the kinetics of tungsten grain growth. Notably, a dependence of water concentration and grain size is emphasized, as evidence suggests that water concentration plays a significant role in modulating the grain size during the reduction process. By considering these factors, we aim to unravel the complex interplay between reduction parameters and grain growth, facilitating a more nuanced understanding of the underlying mechanisms driving the observed GSD evolution and morphology changes in metallic tungsten.

In summary, this study presents a quantitative analysis of GSD evolution and morphology changes in metallic tungsten during hydrogen reduction of tungsten oxides. The obtained results, based on conventional and advanced characterization techniques, provide crucial insights into the growth rates of crystallites and grains within the

metallic phase. By discussing our qualitative and quantitative findings, we contribute to the broader understanding of the mechanisms governing grain growth and microstructural transformations in metallic tungsten. Thus, this study not only advances academic knowledge but also provides practical tools for industry, leading to financial and environmental gains.

2. Experimental methodology

2.1. In-situ reduction monitoring and preparation of samples for characterization

Tungsten trioxide (WO_3) powder, prepared by air oxidation of commercial TBO, was used as the starting material for this study. The resulting sole batch of 5 g of WO_3 powder demonstrated 99.9% purity, as revealed by XRD characterization. The WO_3 reduction process was carried out using two high-end thermogravimetric analyzers: Linseis STA1600 PT simultaneous thermobalance and TA Instruments TGA5500. The reducing agent employed was a level 6.0 mixture of nitrogen and hydrogen gas (95% N_2 and 5% H_2). To assure an inert environment, level 6.0 nitrogen gas was utilized as a protective and flushing gas. The use of a similar gas composition helped to minimize undesired buoyancy changes and their effects during gravimeter measurements. For each reduction experiment, a predetermined mass of 30 mg of tungsten trioxide powder was accurately weighed before deposition onto TGA crucibles with a height of 2 mm. In line with the findings of Estupinan et al. [19,20] obtained through numerical investigations of TGA setups, we intentionally opted for minimal powder beds in our experimental setup, where the employed powder bed exibed a height of approximately 0.4 mm. This ensures consistent and uniform reaction conditions with optimal H_2 penetration, referenced to the theoretic reaction rates of the different steps, while circumventing any possible complications arising from localized water vapor retention.

The influence of powder bed height on the gas species distribution and product retention is notable. Lower powder beds create a more uniform distribution of gas species and minimize product retention. This phenomenon is a result of a complex interplay of factors, particularly the higher water release due to increased reduction temperatures and the interactions between the powder bed setup and gas inflow rates. Augmented powder bed heights enhance re-circulation, impeding the effective evacuation of H_2O [19]. Thus, in the selected setup for this research, diffusion mechanisms are not a limiting factor allowing us to gain closer understanding of kinetic mechanisms of the process.

According to the employed TGA apparatus, reduction processes were performed at low temperatures (i.e., <850 °C) using platinum crucibles and high temperatures (i.e., >850 °C) using alumina crucibles. To minimize any potential contamination and to ensure the integrity of the reduction process, the reducing chamber was always thoroughly evacuated to a high vacuum prior to experimentation. In-situ monitoring of the reduction process was conducted to track the mass loss. By instantly monitoring mass loss, the reduction progress was determined and aimed to accurately prepare samples for further characterization at specific points of the reduction process. For preparing the samples representatives of specific reduction progress, the reducing agents were first stopped and the reducing chamber was flushed with the inert gas. This flushing step ensured the removal of any residual reducing agents. Subsequently, the chamber was cooled down to room temperature and samples were extracted at different desired points of the reduction process. By employing this in-situ monitoring approach and extracting samples at various stages of the reduction process, we were able to capture the transient evolution of the reduction process to investigate the grain growth and morphology changes by a subsequent comprehensive characterization. To investigate the influence of temperature on the grain size evolution, reduction experiments were isothermally conducted at 750 °C, 800 °C, 850 °C, and 900 °C. Similarly, to explore the influence of humidity, reduction experiments were performed at 850 °Cand 900 °Cunder four different H_2 to H_2O concentrations. Reacting gases were only applied during the isothermal holding time. The control of humidity levels was achieved by mixing the reducing gas (N_2/H_2) and a water carrier gas (N_2/H_2O), with volume flow rates herein defined as $\dot{H}_2$-carrier and $\dot{H}_2O$-carrier respectively. The latter gas was volume flow controlled at 2, 4, and 8 Nl h^{-1}, enabling us to observe the influence of humidity on the tungsten grain size evolution. The water carrier gas, $\dot{H}_2O$-carrier, was obtained by passing pure nitrogen through water column humidification, until saturation at ambient temperature, allowing regulation of the water vapor concentration. Drawing on the study conducted by Vasu et al. [21], we have undertaken an evaluation of relative humidity (RH) measurements within our humidification system. These measurements spanned a range of flow rates, specifically targeting $\dot{H}_2O$-carrier at 2, 4, and 8 Nl h^{-1}, as utilized in our experimental campaigns. The results consistently indicated an RH of about 80 % ± 5 % across all experimental conditions. This uniformity in RH allows us to assume a constant inlet humidity level throughout the course of our experiments. In accordance with the ideal gas law under standard conditions, we have computed the partial pressures of the reactive species. The partial pressures for water vapor (P_{H_2O}) were found to be 521 ± 31, 868 ± 54, and 1302 ± 81 Pa for $\dot{H}_2O$-carrier equal to 2, 4, and 8 Nl h^{-1}, respectively. In contrast, the hydrogen partial pressures (P_{H_2}) were calculated to be 4053, 3377, and 2533 Pa for the same respective $\dot{H}_2O$-carrier flow rates. It should be emphasized that the observed stability in humidity levels is primarily influenced by the consistent flow rate of the water carrier gas. This aspect of our methodology ensures that variations in system humidity are directly proportional to the changes in the volume flow of the water carrier gas, highlighting the efficacy of our control measures in maintaining desired humidity conditions.

2.2. Characterization of samples

X-ray diffraction (XRD)

Post-reduction specimens collected from the samples prepared in the thermogravimetric analyzers were carefully prepared for X-ray diffraction (XRD) analysis using the multi-purpose X-ray diffractometer Bruker D8. The XRD profiles were obtained for identification and quantification of crystalline phases in the samples using Cu-Kα radiation with wavelength $\lambda = 1.54$ Å. Software-assisted analysis techniques, such as Rietveld refinement for structural analysis [22] and Whole Powder Pattern Modeling (WPPM) [23,24] for microstructural analysis, were employed to extract detailed information on the relative composition and crystallite size distribution of the formed tungsten. Rietveld refinement provided precise information on the relative amounts of metallic tungsten and any remaining oxide phases. Additionally, WPPM [23–25] allowed mean crystallite size analysis evolution of the involved tungsten and oxide phases. By utilizing these techniques, a better understanding of the crystalline structure and the mean crystallite size characteristics of the formed tungsten was obtained.

Electron microscopy

Energy-Dispersive X-ray Spectroscopy (SEM-EDS) was performed on the samples to facilitate the identification of the formed metallic phase and, to some extent, the determination of its Grain Size Distribution (GSD). As is well known, employing SEM-EDS maps is not ideal for quantifying oxide content. While EDS can detect oxygen, performing a quantitative analysis on this element may be erroneous due to, e.g., self-absorption, and limitations in detector efficiency [26]. However, an EDS analysis at selected points, on the sample surface, can provide more reliable information on the non-presence of oxygen in the vicinity of analysis points. This facilitate the selection of pure tungsten grains for further size estimation. Additionally, Transmission Electron Microscopy (TEM) was employed to obtain higher-resolution imaging. The combination of SEM-EDS and TEM techniques allowed for a basic understanding of the microstructure evolution of the samples and the formation of the metallic tungsten phase.

Synchrotron study

State-of-the-art synchrotron X-ray phase contrast nano-holo-tomography (XNH) at the European Synchrotron Radiation Facility (ESRF) was employed to obtain three-dimensional (3D) images of individual tungsten agglomerates. The high-resolution phase contrast images were acquired at the ESRF beamline ID16B [27]. Each XNH scan consists of 4 tomography scans at different focus-to-object distances. For each tomography scan, two-dimensional (2D) projections with a pixel size of 25 nm are acquired at 29.6 kV. In-house algorithms of phase retrieval and filtered back-projection provide a 3D reconstructed volume of the sample. To enhance the robustness of our results, a double scanning the samples was employed when necessary, primarily due to undesired sample movements and adjustments in instrument parameters. This method, although commonplace, significantly enhances the repeatability and reliability of our measurements. This magnified phase contrast imaging technique provided a fine 3D characterization of the microstructure [27,28], enabling the assessment of the actual volume morphology and size evolution of individual tungsten grains within the precursor oxide matrix.

The post-processing of the reconstructed XNH data was performed using deep learning algorithms within the Dragonfly-ORS software [29]. Following a similar procedure as described in [30], three random image slices were selected from each reconstructed volume. These selected images were then employed for user-assisted training of the model, specifically focusing on denoising, segmentation, and boundary recognition. Consequently, the model was applied to the remaining images of the reconstructed volumes. This approach enabled the efficient and accurate identification of phases and grain boundaries within the microstructure. These advanced post-processing techniques, though pioneering when applied to reconstructed XNH data, in combination with our meticulous methodology, facilitated the precise measurement of the tungsten grain size distribution in each sample. This process underlines the reliability of our findings and underscores the innovative application of these techniques in our research field.

3. Results

3.1. Hydrogen reduction of WO_3

Under each specific reduction condition, full reductions were meticulously conducted and repeated to ensure the repeatability of each reduction sequence. Herein, we define a reacting holding time as the time in which the isothermal reduction temperature in the presence of reacting gases was kept. Fig. 1 presents the TGA curves of experiments conducted under a dry atmosphere at four different temperatures. These TGA observations under dry conditions align with the findings reported in previous studies [5,6,18,31]. Additionally, similar experiments were performed under four different humidity conditions. Fig. 2 provides a comparison of the complete reduction sequence for the various employed humidities. The inflection points observed in the TGA curves (refer to Figs. 1 and 2) suggest changes in the phase composition of the sample, as each reduction step exhibits its own characteristic reaction kinetics [4]. This method of interpreting TGA inflection points in terms of phase composition alterations is made feasible by our thorough understanding of the process chemistry and of our specific experimental setup. Such an approach aligns with the conclusions of [18], indicating that the reduction experiments were not constrained by diffusion mechanisms. As observed in all the TGA experimentation, for the chosen reduction conditions, there is almost no distinguishable difference in the initial part of the reduction, specifically in the range covering the steps $WO_3 \longrightarrow WO_2$. This similarity holds even more in experiments performed at the same isothermal temperatures but under different humidities (i.e., Fig. 2). However, notable differences become apparent during the final step of the reduction, where variations in the H_2/H_2O ratio exert a more pronounced influence in longer reduction steps delaying the reaction progress. In contrast, the influence of temperature on the reactions rate (i.e., Fig. 1) is observable right from the start of the reaction.

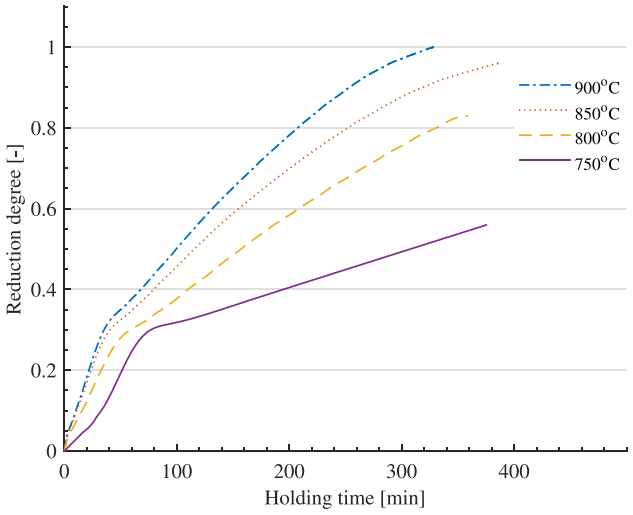

Fig. 1. Influence of temperature on the H_2 reduction of WO_3 - Isothermal TGA reduction curves under dry atmospheres (i.e., N_2/H_2 95/5 = H_2-carrier = 8 Nl h^{-1}) at different temperatures.

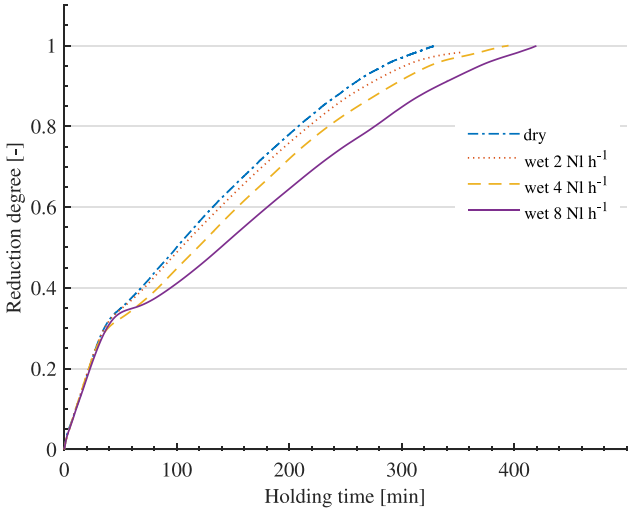

Fig. 2. Influence of humidity on the H_2 reduction of WO_3 - Isothermal TGA reduction curves at 900 °C and four different humidity atmospheres.

As defined in Fig. 3, samples indicatives of the different reduction stages were prepared by repeating the same full reduction experiments shown in Figs. 1 and 2, but with the reaction path stopped at shorter times. Consequently, Fig. 3 illustrates and exemplifies a set of reduction experiments stopped at various reduction degrees. From this experimentation procedure, the obtained samples can be seen as the quasi in-situ representation of the transient evolution of the reduction process. As highlighted with a frame in Fig. 3, the focus of the preparations was given to the $WO_2 \rightarrow W$ step as it is ultimately influencing the final properties of the obtained metallic tungsten. The set of samples, exemplified in Fig. 3, were prepared at 900 °C and under a mixture H_2 and wet-N_2 volume flow controlled at 4 Nl h^{-1}.

While it is not necessary to present all the curves for each reduction experiment conducted and samples prepared in this study, a summary of the various prepared samples and their corresponding experimental conditions can be found in Table 1. For more comprehensive data from

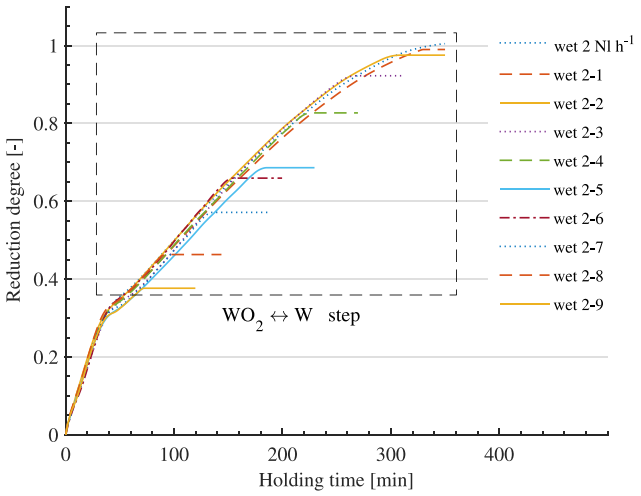

Fig. 3. Thermogravimetric curves, representing isothermal reduction experiments of WO_3, stopped at various reduction degrees. These experiments were conducted at 900 °C, $\dot{H}_2$-carrier = 8 Nl h^{-1} and $\dot{H}_2O$-carrier = 2 Nl h^{-1}. The labels are assigned according to experiment names reported in Table 1; where the first number (2) corresponds to volume flow of the $\dot{H}_2O$-carrier gas.

Table 1
Summary of reaction conditions for TGA experimentation on H_2 reduction of WO_3. During all the experiments the volume flow of the reducing gas H_2 was maintained to 8 [Nl h^{-1}].

Experiment label	Temperature [°C]	H_2O [Nl h^{-1}]	Reduction degree [%]
Dry_750-0 ⋮ Dry_750-3	750	0	52 ⋮ 35
Dry_800-0 ⋮ Dry_800-7	800	0	98 ⋮ 36
Dry_850-0 ⋮ Dry_850-4	850	0	100 ⋮ 35
Dry_900-0 ⋮ Dry_900-9	900	0	100 ⋮ 40.2
Wet_2-0 ⋮ Wet_2-9	900	2	100 ⋮ 39.7
Wet_4-0 ⋮ Wet_4-8	900	4	100 ⋮ 41.8
Wet_8-0 ⋮ Wet_8-9	900	8	98.9 ⋮ 34.1

these experiments, interested readers are welcome to get in touch with the authors.

The composition of each reduction sample was precisely determined using X-ray diffraction (XRD). Fig. 4 illustrates the transient evolution of XRD patterns obtained at the various stages of the reduction process. Notably, the appearance and intensification of peaks corresponding to the newly formed metallic tungsten phase (namely, peaks (110), (200), (211), (230) and (310)) are observed in this figure, as well as in all our collected data. The patterns in Fig. 4 correspond to the reduction conditions of samples "wet_2…" outlined in Table 1. The quantification of the weight percentages for the involved phases is presented in Fig. 5. It is worth highlighting that the measurement error exhibited an increase when analyzing phases with vanishing content. This effect was particularly pronounced due to the relatively low mass of each sample. These challenges stem from inherent limitations of

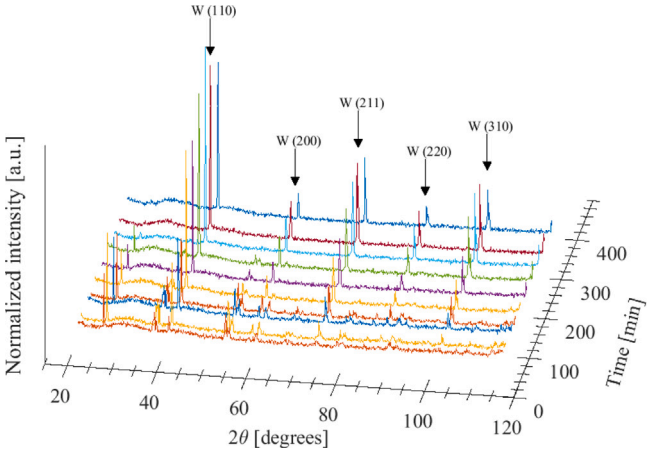

Fig. 4. X-ray Diffraction 3D-plot (2θ-Intensity) characterizing the transient evolution of the hydrogen reduction of WO_3. Reduction at 900 °C and a mixture $\dot{H}_2$-carrier = 8 Nl h^{-1} – $\dot{H}_2O$-carrier = 4 Nl h^{-1}.

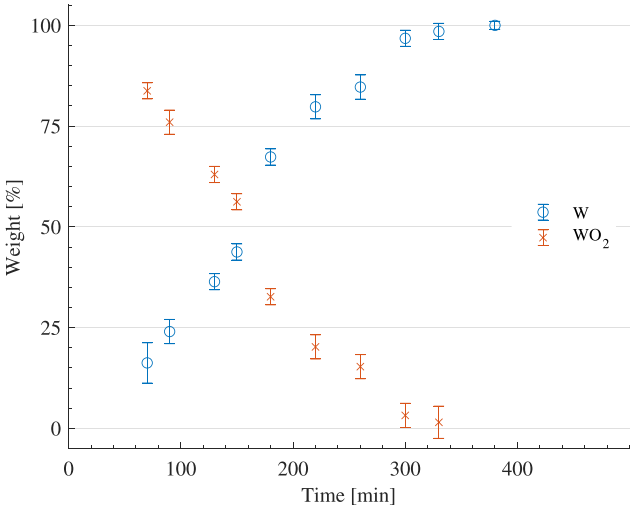

Fig. 5. Illustration of weight percentage evolution of pure tungsten phase and its precursor WO_2 phase during H_2 reduction. Data obtained by Rietveld refinement of the XRD patterns in Fig. 4. The error bars indicate the uncertainty of the refinement.

the instrumentation. However, it is important to underscore that our primary emphasis was on measurements concerning the pure tungsten phase, which consistently maintained relatively higher content in the samples of analysis. As a result, our confidence in the accuracy of these measurements remains substantiated. This holds true for the refinement conducted for mean crystallite size analyses presented later on this paper.

3.2. Morphology evolution upon reduction

In this contribution, we explore three different size lengths. Firstly, crystallites understood as individual crystalline domains. Secondly, we delve into grains, which are clusters of crystallites. Finally, we observe particles, which refer to the individual dense, compact assemblies of tungsten grains.

The morphologies of the fully formed metallic tungsten, as observed in this study, align with numerous investigations previously reported on the reduction of tungsten oxides [4,8,12,13,18,32,33]. In Fig. 6, the SEM images illustrate the distinctive final morphologies resulting from reductions under different conditions. Notably, the so-called pseudo-morph particles [4] persisted in dry experimental conditions, but their

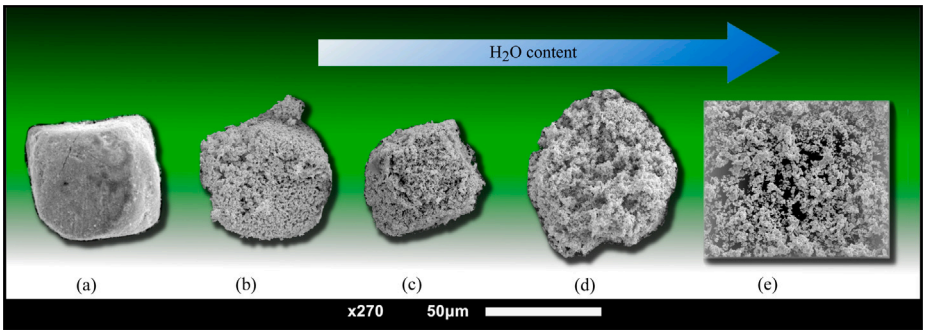

Fig. 6. Schematic representation illustrating the impact of humidity on the morphology of primary particles after complete reduction. Each image has been extracted from the SEM observations of primary particles of the reduced samples. (a) Initial TBO particle, (b) Pseudomorph particle in sample "Dry_900-0", (c) Pseudomorph particle in sample "Wet_2-0", (d) Vanishing pseudomorph particle in sample "Wet_4-0", and (e) Loose grains in sample "Wet_8-0".

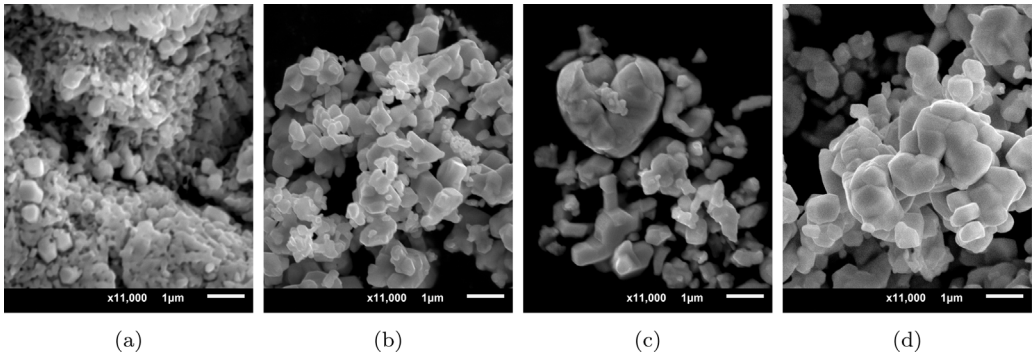

Fig. 7. SEM images describing the impact of temperature and humidity on the morphology of tungsten grains after full reduction: (a) Sample "Dry_800-0", (b) sample "Dry_900-0", (c) sample "Wet_4-0", and (d) sample "Wet_8-0".

presence diminished with increasing water concentrations in the reducing atmospheres. In the course of dry experimentation, there was no significant alteration in the final particle morphology. This observation is in line with the established understanding that, under dry conditions and particularly at lower temperatures, the resulting tungsten powder retains the pseudomorphic characteristics of the original TBO particles (see Fig. 6b). These particles maintain their pseudomorphic form, manifesting as a sponge-like structure that is partially recrystallized into fine grains, as depicted in Figs. 7(a) and 7(b). By introducing water into the reduction process, the gradual disappearance of these pseudomorphous formations takes place. Consequently, larger grains emerge, although they still retain a semblance of pseudomorphism (see Fig. 6d). As the water content increases further, a more loosely structured grain arrangement becomes apparent, accompanied by the absence of pseudomorphous features. In Fig. 7, a comparison of the grain morphology of samples fully reduced under various humidity and temperature conditions can be observed. Finer grains are visible on the fractured surface of primary particles under dry and lower temperature settings (refer to Fig. 7(a)). Additionally, higher reduction temperatures under dry conditions result in the emergence of looser grain structures (see Fig. 7(b)), while increased humidity leads to the formation of larger grains (Figs. 7(c) and 7(d)). As illustrated in Figs. 7(c) and 7(d), a significant degree of crystallization and coalescence is evident, akin to findings from previous experiments by Wu et al. [34]. Notably, this coalescence phenomenon is more pronounced in wet reduction conditions, where the deposition of volatiles contributes to enhancing the growth and coalescence process. With more pronounced H_2O content and higher temperatures, the fracture and CVT are favored, resulting in a looser powder structure describing larger grains.

Owing to the similar grain morphologies of WO_2 and W phases, distinguishing the newly formed tungsten grains for further size measurement can be challenging. As perceived in Fig. 7, the formed tungsten grains often display faceted shapes. Nevertheless, as it can be seen in the same images and as demonstrated in Fig. 8, this is not a consistent feature. As depicted in Fig. 8 through the application of energy-dispersive X-ray spectroscopy (EDS), it is possible to identify pure tungsten grains adopting more rounded shapes, reminiscent of their WO_2 precursor phase. Combining EDS with the SEM and TEM observations can provide valuable insights into the chemical composition of the analyzed samples. However, it is crucial to note that in

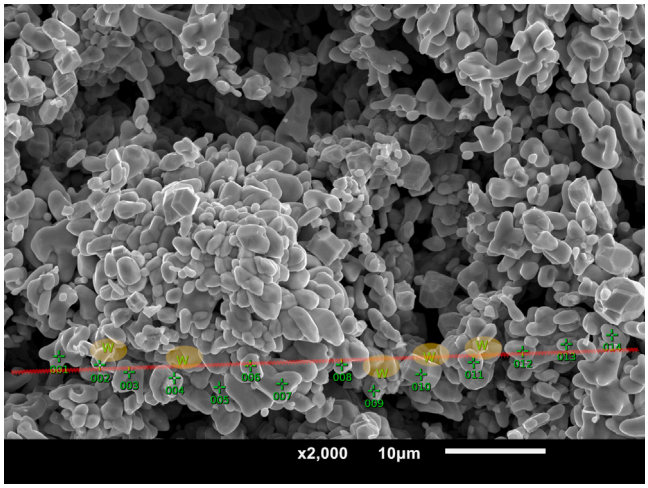

Fig. 8. Illustration of SEM-EDS analysis for a WO_2 particle undergoing H_2 reduction. The chosen points are EDS measurements determining the presence of pure tungsten in the designated grain. These points were selected along a random trajectory for subsequent grain size characterization. The partially reduced oxide particle was extracted from the sample "Wet_8-4".

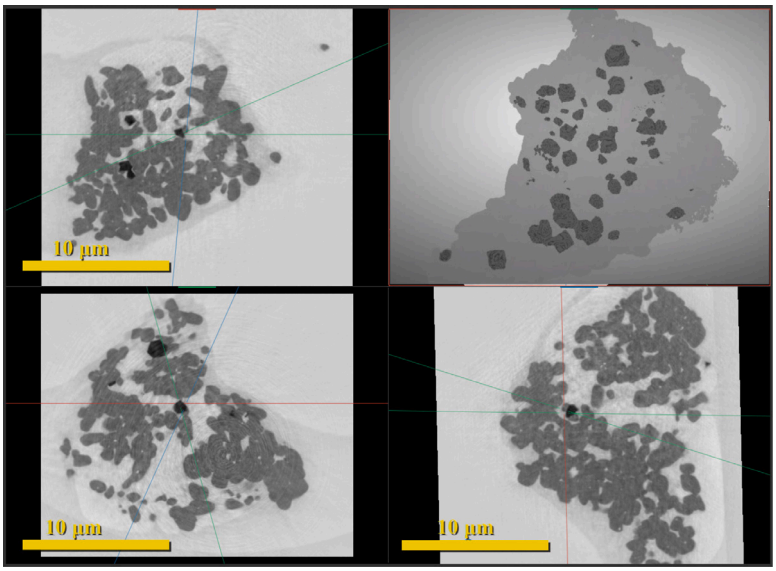

Fig. 9. Synchrotron nano-tomography observation on a partially reduced WO_2 particle during volumetric reconstruction in Dragonfly-ORS [29]. The upper-right figure is the reconstructed volume of the particle, upper-left is the xz-plane section, lower-left is the xy-plane section and lower-right is the yz-plane section. The enabled phase contrast and the high resolution imaging allow the recognition of newly formed tungsten grains and further grain size analysis on the segmented phase can reliably be performed. Distinctive color coding: metallic tungsten grains in black, precursor oxide matrix in gray, and void space in white.

our observations, as introduced in Section 2.2, revealed limitations in employing EDS maps measurements on partially reduced samples, as such measurements yielded misleading information on the oxygen quantities. This limitation became particularly pronounced when observing agglomerates, as the beam penetration detected remaining intraparticle oxide. Consequently, considering the required resolution for grain size characterization and the detector efficiency, EDS analysis was employed solely by manual pointing to grains over a random trajectory (as shown in Fig. 8). As a result, only spots indicating zero oxygen content were reliably included in the size analysis of the samples. This corresponds to samples obtained at almost, or fully, reduced stages. The purpose of the EDS analysis was not to investigate the intermediate oxide phases, but rather to identify pure tungsten grains for subsequent size characterization. It has to be pointed out that, in general, EDS-SEM measurements yield only localized information and may not necessarily represent larger samples in a statistically comprehensive manner. However, in the context of our study, the uniformity of the reduction process within our setup plays a pivotal role in validating our approach. This uniformity is demonstrated by the consistent measurements obtained from random locations across the powder bed in each analyzed sample. Furthermore, the trends observed in our three-dimensional measurements serve to further reinforce the reliability of the information obtained.

While the presence of pseudomorphous particles tends to diminish in wet conditions, a subtle agglomeration of grains can still occur. In our study, for the sake of simplifying sample preparation for synchrotron nano-tomography, we intentionally chose agglomerates approximately 40 µm in size from samples representing various reduction stages. These agglomerates were then subjected to synchrotron X-ray nano-tomography for a more comprehensive understanding of the evolution of the metallic tungsten phase. The computed nano-tomography reconstruction, in contrast to 2D images, granted us access to the complete 3D information of grain sizes, a crucial advantage especially when observing agglomerated particles such as the tungsten pseudomorphs. Additionally, as depicted in Fig. 9, the employed XNH technique facilitated the identification of the tungsten grains of interest addressing the limitations of the SEM-EDS observations mentioned earlier. As a result, our methodology enabled the high resolution observation of the progressive morphology change and a precise grain size quantification within each sample.

Fig. 9 exemplifies and captures the observation process of the high quality synchrotron data. This figure was generated following the filtering and enhancement routines of the reconstructed XNH data. Images featuring scale-bars depict representative sections of the particle captured from three distinct orientations: xz (upper-left), xy (lower-left), and yz (lower-right); while the section xz represents an actual acquired slice, the other displayed sections are image computations from Dragonfly. The upper-right figure showcases the reconstructed volume of the particle. As depicted in the 2D planes of Fig. 9 (e.g., xz-, xy- and yz-section), the obtained data provides a sufficient resolution to capture tungsten grain boundaries and preform a reliable segmentation and size characterization due to the attained sharp edges.

Among the collected nano-tomography data, Fig. 9 has been deliberately selected to show and discuss the early formation of metallic tungsten grains within the oxide particle. Unlike the early emergence of tungsten grains on the particle's surface, as presented in Fig. 10(a), tungsten can initiate its formation inside the particles. This occurrence is made possible thanks to the removal of oxygen during the reduction of intermediate oxides, which results in the formation of porosity and gaps. The small-size H_2 molecules easily diffuse in the intraparticle. Subsequently, hydrogen reacts with the oxide phase inside the particle, leading to the release of H_2O. This water vapor formation within the particle interior contributes to two significant phenomena. Firstly, it can react with the existing oxide phase, generating volatiles that contribute to grain growth via CVT. Secondly, at higher reaction rates, the partial pressure of water vapor rapidly increases, causing heightened stresses at the intraparticle, which lead to fractures. These fractures may promote higher reduction rates as they expose more oxide phase, and they may also contribute to possible tungsten size change contingent upon the specific reduction environment. This particular synchrotron nano-tomography (Fig. 9), was conducted on the "Wet_8-9" sample, where the metallic tungsten phase accounted for only about 14% of the total mass weight. At this stage, the probability of selecting particles with only oxide phases for synchrotron observation is elevated. Thus, our fortunate selection of this particular specimen substantiates and complements previous theories, such as those by Lackner et al. [13] and Kamerovic et al. [33], regarding the fracture of tungsten oxide particles during reduction.

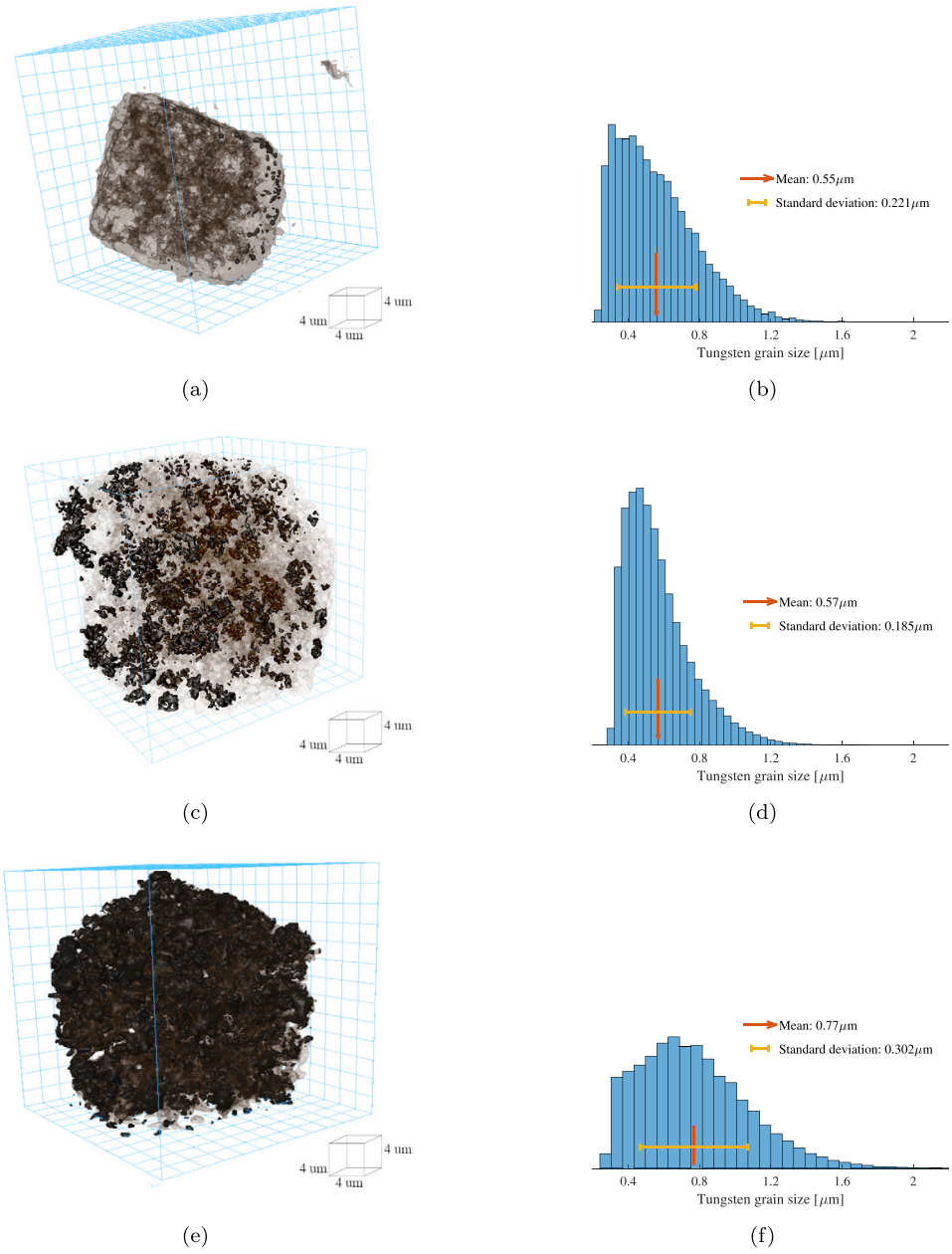

Fig. 10. Visualization of volume reconstructions of synchrotron nano-tomographies illustrating agglomerated particles comprising WO_2 (colored brown) and W(colored black) phases at various stages of the H_2 reduction of WO_3. For each reconstructed volume, a normalized grain size distribution (GSD) histogram is provided, obtained through mean Feret diameter computations on the volumetric reconstruction. (a) Sample "Wet_2-8", 45% reduction progress. (b) GSD for sample "Wet_2-8". (c) Sample "Wet_2-5", 71% reduction progress. (d) GSD for sample "Wet_2-5". (e) Sample "Wet_2-2", 95% reduction progress. (f) GSD for sample "Wet_2-2". For size reference, it should be noted that each cubic cell in the 3D grid containing the particles has a side length of 4 μm.

3.3. Tungsten grain size evolution

By employing the segmented data from the synchrotron nano-tomography reconstructions, we gained high-resolution insights into the grain size distribution (GSD) of metallic tungsten both within particles and on their surfaces. In Fig. 10, we provide a visual illustration, as an example of the synchrotron observations, at three distinct stages of the reduction process. In the figure, the left side displays the volumetric reconstruction of the selected agglomerates, while the right side shows their corresponding normalized GSD. The grain size data was derived from the computation of mean Feret diameter for each identified metallic tungsten grain. In the volumetric reconstructions, after phase contrast segmentation, separated classes for metallic W grains and the precursor WO_2 phase were achieved. Tungsten grains are depicted in black and the WO_2 matrix is shown in brown. The WO_2 phase has been rendered with transparency to facilitate the visualization of intraparticle formation. The light-brown areas may indicate porosity. However, as there is no intention to provide a detailed description of the porosity, the rendering primarily emphasizes the appearance of tungsten within the oxide matrix. The figure clearly depicts the gradual formation and widespread propagation of the W phase within the precursor oxide matrix. From Fig. 10, a noticeable shift of the mean grain size towards larger grains (i.e. from ~0.5 μm to ~0.8 μm), and a wider distribution towards the final points of the process (see Fig. 10(f)), is also evident. The broadening of the distribution is a natural outcome of the transient formation of tungsten grains. As stable tungsten nuclei, formed in the early stages of the reaction, grow over time; tungsten grains, formed at the last stages of the reaction, will tend

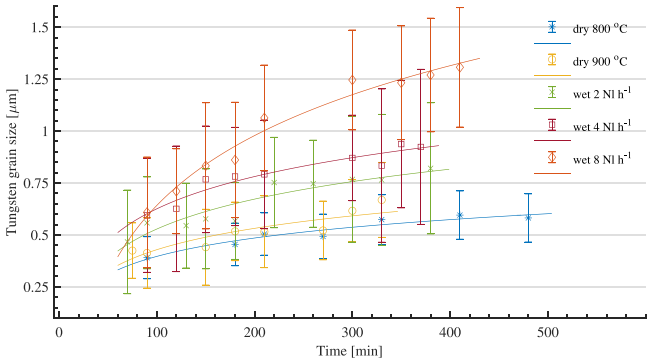

Fig. 11. Transient evolution of tungsten grain size distribution during H_2 reduction of WO_3. Each reduction sample is represented with error bars indicating the mean tungsten size and its corresponding standard deviation. Logarithmic trend lines are overlaid on each reduction curve.

to remain around similar sizes to those of the stable critical nucleus sizes.

For each of the reduction conditions listed in Table 1, we chose representative reduction samples and conducted analogous analyses and data collection processes, similar to what is depicted in Figs. 10(b), 10(d) and 10(f). These analyses were further enriched by 2D data from electron microscopy images, such as the one shown in Fig. 8, primarily captured during the later stages of reduction. By marrying the vast collected data gleaned from both 2D and 3D techniques, we generated a comprehensive overview of the granular landscape, allowing us to quantify and characterize the changing grain sizes throughout the reduction process. As a result, Fig. 11 provides the summary of the acquired data showing the transient evolution of W mean grain size and its distribution throughout the reduction of WO_3 under various reaction conditions. In the plots, the error bars are representative of the statistical spread of the computed grain sizes. It is possible to observe a logarithmic trend of the plotted data versus time. However, there is a linear correlation between the evolution of grain size and the progress of reduction or tungsten formation. This linear trend is further elaborated in Fig. 12, where separate figures illustrate the behavior for dry and wet conditions. Extrapolating the data in the direction of the initial stages of W formation, we can deduce that, for the selected starting oxide powder, the stable critical nucleus size (or the smallest grain) is approximately 0.35 μm for dry reduction conditions. For wet reduction conditions, this size falls within the range of 0.4–0.6 μm. Quantifying these nuclei size and grain growth rates holds significant implications, particularly for nucleation and growth modeling. Another crucial observation, in Fig. 12(a), pertains to the convergence of tungsten grain size evolution under dry conditions. While the mean size exhibits a consistent trend, narrower distributions become apparent at lower reduction temperatures. This phenomenon can be explained by the reduced formation rates of H_2O at lower temperatures, leading to more uniform gas educts diffusion and products evacuation as fewer fractured particles emerge. Consequently, more uniform conditions across the bed are prescribed and the cluster of formed grains experiences a more uniform growth. Conversely, at higher reduction temperatures, as explained earlier, excessive water formation can result in fracture. We hypothesize that certain grains experience elevated growth rates before fracturing, and this trend may allegedly persists afterward akin to an Ostwald ripening mechanism. As a consequence, these occurrences contribute to widening the size distribution under higher reduction temperatures.

In a manner analogous to the provided grain size data, our XRD analyses yielded insights into the evolution of mean crystallite sizes. Fig. 13 compiles the plots depicting the progression of mean crystallite sizes under the various reduction conditions. Notably, as it happens for grain growth, a discernible acceleration in crystallite growth is apparent with higher humidity content. While exploring the connection between the sizes of the generated tungsten crystallites and grains was not the primary focus of this study, the observed data trends do suggest a plausible correlation between growth rates for crystallites and grains. Such a plausible correlation is clearly illustrated in Fig. 14, where plots for the impact of humidity on the mean grain size and the mean crystallite size, of complete reduction experiments conducted at 900 °C, are juxtaposed. The insights gained from this multi-dimensional approach enrich the comprehensive understanding of the dynamics of tungsten formation, growth and their relationship with the reduction conditions.

As a general discussion, complementing the existing literature, let us now extend our perspective to encompass the implications of these grain size results on the overall understanding of the reduction process. Every one of the WO_3 reduction steps (i.e., $WO_3 \rightarrow WO_{2.9} \rightarrow WO_{2.72} \rightarrow WO_2 \rightarrow W$) is followed by the emergence of the intermediate volatile transport phase $WO_2(OH)_2$. This volatile phase is subsequently deposited onto the initial nuclei or newly formed tungsten structures, leading to the emergence of an entirely new grain morphology and GSD in the resulting product. The size distribution of tungsten grains is then intricately influenced by the specific conditions of formation and deposition of this transport phase. Both wet and dry reduction pathways are highly likely to follow this described mechanism. In dry reduction scenarios, grain growth is constrained due to the limited production of volatiles. Lower reduction temperatures result in slower water production rates, and an efficient removal, from the powder bed, of generated water inhibits the formation of volatiles. Nevertheless, even in the most homogeneous and dry reduction conditions, the produced water vapor can be retained at the intraparticle due to the possible formation of tungsten inside the primary particles. This occurrence promotes localized CVT and leads to grain growth.

We did not observe a significant number of large grains as reported in other WO_3 reduction studies [4,18,32]. In these works, average sizes on the order of tens of micrometers can be observed and it can be attributed to localized water vapor retention employed during their experiments. Moreover, contrary to the literature (e.g., Lackner et al. [13]), from our observations it can be inferred that the formation of metallic tungsten occurs only after the complete conversion of the sample into WO_2. These differences on size and early tungsten formation can be attributed to the use of significantly smaller samples in our study. This approach led to a highly uniform setup, characterized by a minimal powder bed, which distinctly influences the reaction dynamics. This configuration facilitates the uniform diffusion of hydrogen into the oxide feedstock, and the produced water is immediately removed by the incoming flow. The imposed environment facilitates increased contact with the incoming reacting agents, further driving oxygen extraction from the oxide particles. Thus, CVT and further grain growth effect is solely attributed to the humidity carried by the reducing gas mixture. As a result, the growth of tungsten grains observed in our study can be unequivocally linked to the influence of incoming water vapor.

4. Conclusion

The comprehensive quasi in-situ analysis of tungsten grain size evolution and morphology changes during the hydrogen reduction of WO_3 has provided valuable insights into the underlying mechanisms governing microstructure transformations. The integration of various advanced characterization techniques has greatly enhanced our understanding of the tungsten oxide reduction process and the evolution of grain sizes. Through computed XNH reconstruction, we were able to access complete three-dimensional information regarding grain sizes, a crucial advantage when examining complex structures like agglomerated particles, such as tungsten pseudomorphs. The phase contrast capability of this technique has also been crucial in identifying and segmenting the tungsten grains of interest, addressing challenges posed

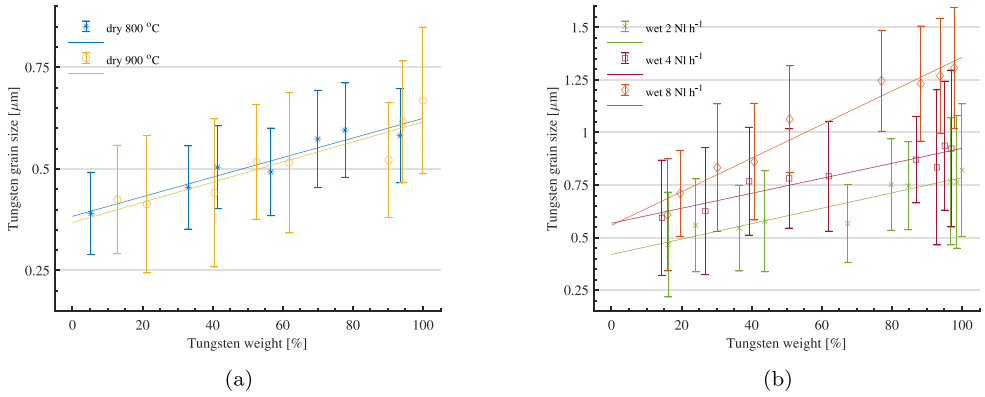

Fig. 12. Comparison of tungsten grain size changes during tungsten formation via H_2 reduction of WO_3. Error bars represent the mean tungsten size and its corresponding standard deviation. Linear trend lines are superimposed on each reduction curve. (a) Reductions under dry conditions. (b) Reductions under wet conditions.

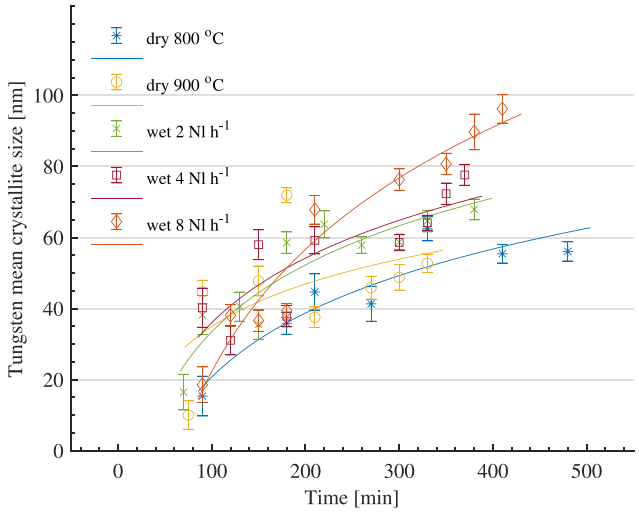

Fig. 13. Transient evolution of tungsten mean crystallite size during H_2 reduction of WO_3. Error bars represent the uncertainty in WPPM computation [25]. Logarithmic trend lines are superimposed to each reduction curve.

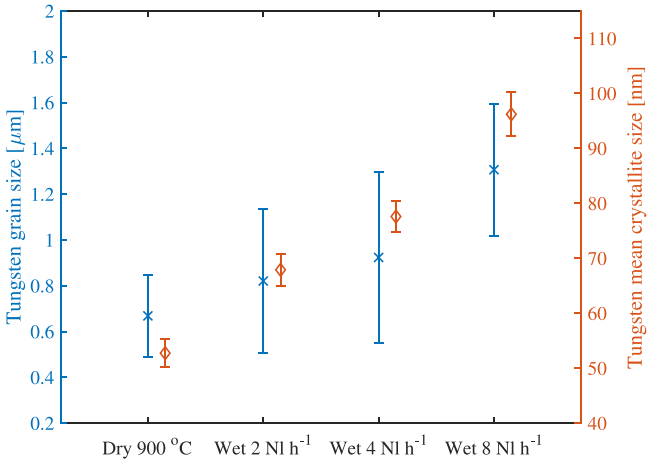

Fig. 14. Comparison of tungsten grain size and crystallite size in samples fully reduced under varied humidity conditions.

by SEM-EDS observations. This approach not only allowed us to observe the progressive formation of tungsten grains but also facilitated precise 3D quantification of the grain size distribution within each sample. Moreover, by utilizing nano-tomography volumetric reconstructions, we were able to accurately estimate W grain sizes at both intraparticle and particle surface, operating at the grain level. Additionally, the integration of 2D data from electron microscopy images enriched our grain size information further. The combination of the employed 2D and 3D imaging techniques as well as the XRD analysis provided a comprehensive perspective on the changing grain and mean crystallite sizes throughout the H_2 reduction of tungsten oxides process. The presented insights are particularly significant for nucleation and growth modeling of metallic tungsten synthesis under industrial conditions, providing quantification of stable tungsten nuclei sizes and growth rates under different reduction conditions.

Based on our observations within the selected experimental range, it can be deduced that tungsten oxide particles undergo fracturing exclusively after the creation of tungsten grains. This phenomenon is particularly evident when metallic tungsten forms at the intraparticle, its grain growth and the accumulating water partial pressure generate stresses precipitating early tungsten-induced fractures.

Our findings also highlight the paramount role of H_2O-content in shaping both the morphology and tungsten grain size distribution. The chosen minimal powder bed setup uniquely enables us to directly link the effect of the incoming water content with the increase of grain growth rate during the synthesis of metallic tungsten. This quantifiable relationship between water content and grain growth emphasizes the pivotal role of humidity in driving the formation and evolution of tungsten grains.

In summary, our quasi in-situ study contributes to a nuanced understanding of the intricate mechanisms governing tungsten grain evolution during reduction. Our approach of using significantly smaller sample sizes than typically employed in experiments has allowed for more intrinsic observations of the process. While existing literature often relies on estimations from bulk measurements, our study provides direct measurements of grain size evolution and morphology changes. These findings not only deepen our knowledge of the metallic tungsten formation via hydrogen reduction of tungsten oxides but also align with kinetic observations reported in the literature, providing a more granular perspective. This direct approach, combined with the comprehensive use of advanced characterization techniques, offers valuable insights and a quantified foundation for more accurate modeling and predictive theory of grain growth dynamics in similar reduction scenarios.

CRediT authorship contribution statement

Alvaro A. Estupinan-Donoso: Conceptualization, Data curation, Formal analysis, Funding acquisition, Investigation, Methodology,

Project administration, Software, Supervision, Validation, Visualization, Writing – original draft, Writing – review & editing. **Pauline Gravier:** Investigation, Writing – original draft. **Rodrigo U. Ichikawa:** Investigation, Software, Writing – original draft. **Andreas Michels:** Methodology, Resources, Writing – original draft.

Declaration of competing interest

The authors declare the following financial interests/personal relationships which may be considered as potential competing interests: Alvaro A. ESTUPINAN DONOSO reports financial support was provided by Luxembourg National Research Fund. If there are other authors they declare that they have no known competing financial interests or personal relationships that could have appeared to influence the work reported in this paper.

Data availability

Data will be made available on request.

Acknowledgments

This work is part of the TuCaNG project funded by the National Research Fund of Luxembourg (Grant 13564670). We acknowledge the for provision of synchrotron radiation facilities under experiment number IM62 on beamline ID16B.

The authors gratefully acknowledge the support provided throughout this research by Ceratizit Luxembourg S.A in particular to Dr. F. Hippe, Dr. I. Peral from the University of Luxembourg, Dr. X. Turrillas from the Institute of Materials Science of Barcelona (ICMAB-CSIC) and the Thermal Engineering research group of the University of Twente in particular to Dr. M. Shahi and Dr. A. Mahmoudi.

Appendix A. Supporting information

Supporting information is available from the author. Three-dimensional animations are available from the Wiley Online Library.

References

[1] K. Mannesson, WC Grain Growth During Sintering of Cemented Carbides (Phd. dissertation), Royal Institute of Technology, Stockholm, Sweden, 2011.

[2] A.A. Estupinan Donoso, Computational study of the industrial synthesis of tungsten powders, Powder Technol. 344 (2019) 773–783, http://dx.doi.org/10.1016/j.powtec.2018.12.065.

[3] E. Lassner, W.-D. Schubert, Tungsten blue oxide, Int. J. Refract. Met. Hard Mater. 13 (1–3) (1995) 111–117, http://dx.doi.org/10.1016/0263-4368(95)00005-4, URL http://linkinghub.elsevier.com/retrieve/pii/0263436895000054.

[4] E. Lassner, W.-D. Schubert, Tungsten: Properties, Chemistry, Technology of the Elements, Alloys, and Chemical Compounds, first ed., Plenum Publishers, 1999.

[5] M.I. Zaki, N.E. Fouad, S. Mansour, A.I. Muftah, Temperature-programmed and X-ray diffractometry studies of hydrogen-reduction course and products of WO3 powder: Influence of reduction parameters, Thermochim. Acta 523 (1–2) (2011) 90–96.

[6] N.E. Fouad, K. Attyia, M.I. Zaki, Thermogravimetry of WO3 reduction in hydrogen: Kinetic characterization of autocatalytic effects, Powder Technol. 74 (1) (1993) 31–37.

[7] Y. Wang, B.F. Long, C.Y. Liu, G.A. Lin, Evolution of reduction process from tungsten oxide to ultrafine tungsten powder via hydrogen, High Temp. Mater. Process. 40 (1) (2021) 171–177.

[8] V. Sarin, Morphological changes occurring during reduction of WO3, J. Mater. Sci. (1975) 593–598, URL http://link.springer.com/article/10.1007/BF00566566.

[9] T.R. Wilken, W.R. Morcom, C.A. Wert, J.B. Woodhouse, Reduction of tungsten oxide to tungsten metal, Metall. Trans. 7B (December 1976) (1976) URL http://link.springer.com/article/10.1007/BF02698592.

[10] P. Taskinen, M.H. Tikkanen, On the reduction of tungsten oxides. Part I. Morphological aspects, Scand. J. Metall. 6 (1977) 223–227.

[11] P. Taskinen, M.H. Tikkanen, On the reduction of tungsten oxides. Part II. Kinetics, Scand. J. Metall. (1977) 228–232.

[12] Y. Wu, Z. Lv, H. Sun, J. Dang, Production of different morphologies and size of metallic W particles through hydrogen reduction, J. Mater. Res. Technol. 8 (5) (2019) 4687–4698, http://dx.doi.org/10.1016/j.jmrt.2019.08.014.

[13] A. Lackner, A. Filzwieser, P. Paschen, W. Köck, On the reduction of tungsten blue oxide in a stream of hydrogen, Int. J. Refract. Met. Hard Mater. 14 (1996) 383–391.

[14] G. Belton, R. McCarron, The volatilization of tungsten in the presence of water vapor, J. Phys. Chem. (1964) 1852–1856, URL http://pubs.acs.org/doi/abs/10.1021/j100789a030.

[15] O.O. Matviichuk, V.P. Bondarenko, A.V. Galkov, O.V. Ievdokymova, Kinetics of transport of WO3 via gas phase, in: Materials Science of Refractory Compounds, at Kyiv, Ukraine, Vol. 4, National Technical University of Ukraine, Kyiv, 2014, p. 1.

[16] M. Ostermann, V. Dalbauer, W.D. Schubert, R. Haubner, Preparation of nano-crystalline tungsten powders from gaseous WO2(OH)2, Tungsten 4 (1) (2022) 60–66, http://dx.doi.org/10.1007/s42864-021-00118-1.

[17] M. Ostermann, R. Haubner, Deposition of nano-crystalline tungsten carbide powders from gaseous WO2(OH)2, Tungsten 5 (1) (2023) 136–144, http://dx.doi.org/10.1007/s42864-022-00142-9.

[18] P. Schoderböck, The reduction of tungsten-VI-oxide to tungsten: A thermogravimetric microscale study with focus on the intermediates, Thermochim. Acta 707 (November 2021) (2022) http://dx.doi.org/10.1016/j.tca.2021.179113.

[19] A.A. Estupinan Donoso, B. Peters, XDEM used for predicting tungsten-oxide reduction, in: Eugeny Kenig (Ed.), Computer Aided Process Engineering (CAPE) Forum 2015, Paderborn, DE, 2015, pp. 43–52.

[20] A.A. Estupinan Donoso, F. Hippe, B. Peters, R. Useldinger, A.A.R. Wilmes, A numerical representation of the industrial production of tungsten powders, in: 19th Plansee Seminar 2017, 2017, pp. 1–12.

[21] G. Vasu, A.K. Tangirala, B. Viswanathan, K.S. Dhathathreyan, Continuous bubble humidification and control of relative humidity of h 2 for a PEMFC system, Int. J. Hydrogen Energy 33 (2008) 4640–4648, http://dx.doi.org/10.1016/j.ijhydene.2008.05.051.

[22] H.M. Rietveld, A profile refinement method for nuclear and magnetic structures, J. Appl. Crystallogr. (1969) http://dx.doi.org/10.1107/s0021889869006558.

[23] P. Scardi, M. Leoni, Whole powder pattern modelling, Acta Crystallogr. Sect. A 58 (2) (2002) 190–200, http://dx.doi.org/10.1107/S0108767301021298.

[24] P. Scardi, Chapter 13. Microstructural properties: Lattice defects and domain size effects, in: R.E. Billinge, S.J.L. Dinnebier (Eds.), Powder Diffraction: Theory and Practice, The Royal Society of Chemistry, Cambridge, 2008, pp. 376–413, http://dx.doi.org/10.1039/9781847558237-00376.

[25] P. Scardi, C.L. Azanza Ricardo, C. Perez-Demydenko, A.A. Coelho, Whole powder pattern modelling macros for TOPAS, J. Appl. Crystallogr. 51 (6) (2018) 1752–1765, http://dx.doi.org/10.1107/S160057671801289X.

[26] E.C. Buck, Electron Microscopy Characterization of Suspended Solids from Hanford Tank 241-AP-105 Direct Feed Waste, Tech. Rep., Pacific Northwest National Laboratory, Richland, Washington, 2017, p. 36, http://dx.doi.org/10.2172/1598866, URL https://www.osti.gov/biblio/1598866.

[27] G. Martinez-Criado, J. Villanova, R. Tucoulou, D. Salomon, J.-P. Suuronen, S. Labouré, C. Guilloud, V. Valls, R. Barrett, E. Gagliardini, Y. Dabin, R. Baker, S. Bohic, C. Cohen, J. Morse, ID16b: a hard X-ray nanoprobe beamline at the ESRF for nano-analysis, J. Synchrotron Radiat. 23 (1) (2016) 344–352, http://dx.doi.org/10.1107/S1600577515019839.

[28] Peter Cloetens, Wolfgang Ludwig, José Baruchel, Jean-Pierre Guigay, Petra Pernot-Rejmánková, Murielle Salomé-Pateyron, Michel Schlenker, Jean-Yves Buffière, Eric Maire, Gilles Peix, Hard x-ray phase imaging using simple propagation of a coherent synchrotron radiation beam, J. Phys. D: Appl. Phys. 32 (10A) (1999) A145, http://dx.doi.org/10.1088/0022-3727/32/10A/330.

[29] Object Research Systems (ORS) Inc, Dragonfly 2020.2, 2020, URL http://www.theobjects.com/dragonfly.

[30] A. Badran, D. Marshall, Z. Legault, R. Makovetsky, B. Provencher, N. Piché, M. Marsh, Automated segmentation of computed tomography images of fiber-reinforced composites by deep learning, J. Mater. Sci. 55 (34) (2020) 16273–16289, http://dx.doi.org/10.1007/s10853-020-05148-7.

[31] R. Haboury, U. Pal, P. Zink, S. Gopalan, S. Basu, Study of an energy storage and recovery concept based on the W/WO3 redox reaction: Part I. Kinetic study and modeling of the WO3 reduction process for energy storage, Metall. Mater. Trans. B 43 (4) (2012) 1001–1010, http://dx.doi.org/10.1007/s11663-012-9656-0.

[32] X.-W. Wu, J.-S. Luo, B.-Z. Lu, C.-H. Xie, Z.-M. Pi, M.-z. Hu, T. Xu, G.-G. Wu, Z.-M. Yu, D.-Q. Yi, Crystal growth of tungsten during hydrogen reduction of tungsten oxide at high temperature, Trans. Nonferr. Met. Soc. China 19 (2009) 785–789.

[33] Z. Kamberovic, D. Filipovic, K. Raic, M. Tasic, Z. Andic, M. Gavrilovski, Reduction of ultra-fine tungsten powder with tungsten (VI)-oxide in a vertical tube reactor, in: MTAEC9, Vol. 45, 2011, pp. 27–32.

[34] C. Wu, Preparation of ultrafine tungsten powders by in-situ hydrogen reduction of nano-needle violet tungsten oxide, Int. J. Refract. Met. Hard Mater. 29 (6) (2011) 686–691.